Linear and weakly nonlinear analysis of doubly diffusive vertical slot convection

Y. Young and R. Rosner
Department of Astronomy and Astrophysics, The University of Chicago, 5640 South Ellis Avenue, Chicago, Illinois 60637
(Received 22 September 1997; revised manuscript received 6 April 1998)

We consider vertical slot convection in the doubly diffusive case over the full range of thermal and solute Rayleigh numbers. We quantitatively categorize the various instability regimes in the linear analyses. In the weakly nonlinear analyses, we derive the amplitude equations using the method of normal forms and study the stability of the finite-amplitude solutions. We discuss in some detail the physics of the various instabilities found in our analyses. [S1063-651X(98)11905-0]

PACS number(s): 47.20.Bp

I. INTRODUCTION

Laterally driven diffusive convection, often referred to as ''slot convection,'' has been the subject of considerable interest over the years ([1–7] and references therein), and is a problem of interest in realms as distinct as convection in stellar magnetic flux tubes and heat transport within insulating double-paned glass windows. Results from linear analyses provide a partial understanding of the experiments [1,8], such as the critical Rayleigh numbers and the width of layer formed. However, linear analysis is incapable of explaining more complex features of the phenomenology. For example, the existence of an equilibrium state at supercriticality can easily be explained by means of weakly nonlinear analysis [2,5], via the existence of a stable finite-amplitude solution, and the fact that the circulation of adjacent convection cells observed in slot convection has the same sign, as pointed out in [1], cannot be explained in linear analysis, but can be understood easily by superposing the finite-amplitude solution with the unperturbed background field [5]. However, finite amplitude analysis in the multiply diffusive case has only been carried out in the asymptotic regime of large solute Rayleigh numbers [5]. The purpose of this paper is to remedy this limitation, and to provide a more complete picture of multiply diffusive slot convection from both linear and weakly nonlinear studies of the system.

We consider a vertical slot that is characterized by an imposed horizontal temperature difference and filled with a solution vertically stratified by addition of a diffusive contaminant. At the outset of the analysis [3,6,7], a vertical shear flow is required to maintain the background steady state, and the constant vertical solute gradient is rendered stabilizing. For large solute Rayleigh numbers [3,5], thin boundary layers develop near the sidewalls, and the fluid remains static in the interior; hence the initially unperturbed state can be well approximated by a quasistatic state, and the instability is double diffusive in nature. Hart [5] investigated the stability of the amplitude equations within the quasistatic approximation in this large solute Rayleigh number regime, and found the properties of the critical states as a function of the solute Rayleigh number for given vertical wave numbers. For small solute Rayleigh numbers, the vertical solute gradient has no stabilizing effect as far as the background shear flow is concerned, and instabilities set in at the same critical thermal Rayleigh number and vertical wave number as those in vertical slot convection [2,9]. For solute Rayleigh numbers between these two extremes, instabilities are oscillatory in nature (Hopf bifurcations), and destabilization is induced by the balance between the background shear flow and the buoyancy oscillations of the fluid [7]. In this regime of solute Rayleigh numbers, the weakly nonlinear analysis of this system becomes quite complicated and has not as yet been undertaken. In this paper we remedy this omission, and perform both linear and weakly nonlinear analyses for multiply diffusive slot convection over a wide range of solute Rayleigh numbers and diffusivity ratios. One of our goals is to provide a complete understanding of the physics underlying multiply diffusive slot convection over the full range of physically plausible conditions. Among the two (alternative, but related) analytical methods for the derivation of the amplitude equations in weakly nonlinear analysis (amplitude expansion and method of normal forms), the method of normal forms is more straightforward when more than two scales are involved in the expansions; for this reason, we use the method of normal forms to analyze the weakly nonlinear behavior near the critical points.

The structure of this paper is as follows: In Sec. II we formulate the problem, describe the methods used in both linear and nonlinear analyses, and present the amplitude equations derived via the method of normal forms. In Sec. III we present an exploration of the control parameter space (defined by the solute Rayleigh numbers). We discuss our results and compare them with earlier work for thermohaline convection [10] in Sec. IV, and provide our conclusions in Sec. V.

II. FORMULATIONS AND METHODS

A. Linear stability analysis

We consider an infinitely tall two-dimensional (2D) channel of width d, as shown in Fig. 1, which we assume to be filled by an incompressible fluid (the horizontal and vertical velocity components can be related to a stream function ψ, $u=\partial_z\psi$; $w=-\partial_x\psi$, respectively); and impose a temperature difference across the channel, of amplitude ΔT. Furthermore, the fluid is initially characterized by a uniform vertical solute concentration gradient, $|\partial_z S_0|$. We shall allow for buoyancy effects, so that we work within the Boussinesq approximation [11]. The Boussinesq equations we shall work with are nondimensionalized by scaling all velocities by

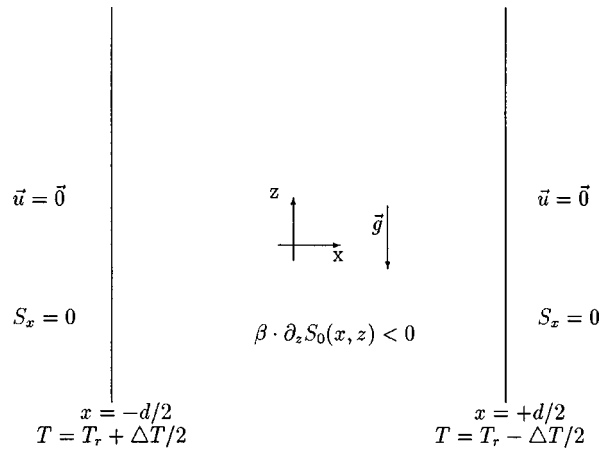

FIG. 1. Sketch of the vertical slot filled with stably stratified solute: $\beta\partial_z S_0 = \text{const} < 0$.

$g\alpha\Delta T d^2/8\nu$ (which is the magnitude of the background shear flow speed), all lengths by $d/2$, temperatures by $\Delta T/2$, the solute concentration by the vertical concentration difference $\Delta S/2 \equiv (d/2)|\partial_z S_0|$, and time by $4\nu/g\alpha\Delta T d$ (which is the circulation time for the background shear flow for a cell of size $d/2$); the resulting governing equations are then given by

$$\left(\partial_t - \frac{16}{\mathrm{Gr}}\nabla^2\right)\nabla^2\psi + \frac{16}{\mathrm{Gr}}\left(\partial_x T - \frac{\mathrm{Gr}_s}{\mathrm{Gr}}\partial_x S\right) = J(\psi, \nabla^2\psi), \tag{2.1}$$

$$\left(\partial_t - \frac{16}{\mathrm{Gr}}\frac{1}{\mathrm{Pr}}\nabla^2\right)T = J(\psi, T), \tag{2.2}$$

$$\left(\partial_t - \frac{16}{\mathrm{Gr}}\frac{1}{\mathrm{Pr}_s}\nabla^2\right)S = J(\psi, S). \tag{2.3}$$

Here $J(f,g) \equiv \partial_x f \partial_z g - \partial_z f \partial_x g$ is the Jacobian; Gr is the thermal Grashof number $g\alpha\Delta T d^3/\nu^2$; Gr_s is the solute Grashof number $g\beta\Delta S d^3/\nu^2$; Pr is the thermal Prandtl number ν/κ_t, and Pr_s the solute Prandtl number ν/κ_s (the thermal Rayleigh number and the solute Rayleigh number are then defined by the expressions $\mathrm{Ra} \equiv g\alpha\Delta T d^3/\nu\kappa_t = \mathrm{Gr}\times\mathrm{Pr}$ and $\mathrm{Ra}_s \equiv g\beta\partial_z S_0 d^4/\nu\kappa_s = -\mathrm{Gr}_s \times \mathrm{Pr}_s < 0$, respectively). The dimensional constants are the thermal expansion coefficient α, the solute volumetric expansion coefficient β, the thermal diffusivity κ_t, the solute diffusivity κ_s, the kinematic viscosity ν, and the gravitational acceleration g. The boundary conditions at the vertical walls are assumed to correspond to impenetrable, no-slip walls fixed at constant temperature (Fig. 1). We also assume the background state (denoted by 0) to be steady and independent of z:

$$\partial_x^4\psi_0 - \partial_x T_0 + \frac{\mathrm{Gr}_s}{\mathrm{Gr}}\partial_x S_0 = 0, \tag{2.4}$$

$$\partial_x^2 T_0 = 0, \tag{2.5}$$

$$\frac{16}{\mathrm{Gr}}\frac{1}{\mathrm{Pr}_s}\partial_x^2 S_0 - \partial_x\psi_0 = 0. \tag{2.6}$$

The unperturbed background fields, i.e., solutions (S_0, T_0, ψ_0), satisfying Eqs. (2.4)–(2.6) are found in [3,6,7]. The linearized perturbed equations are then

$$\partial_t\nabla^2\psi - \partial_x\psi_0\partial_z\nabla^2\psi + \partial_x\nabla^2\psi_0\partial_z\psi + \frac{16}{\mathrm{Gr}}\left(\partial_x T - \frac{\mathrm{Gr}_s}{\mathrm{Gr}}\partial_x S\right) - \frac{16}{\mathrm{Gr}}\nabla^4\psi = 0, \tag{2.7}$$

$$\partial_t T - \partial_x\psi_0\partial_z T + \partial_x T_0\partial_z\psi - \frac{16}{\mathrm{Gr}}\frac{1}{\mathrm{Pr}}\nabla^2 T = 0, \tag{2.8}$$

$$\partial_t S - \partial_x\psi_0\partial_z S + \partial_x S_0\partial_z\psi - \partial_z S_0\partial_x\psi - \frac{16}{\mathrm{Gr}}\frac{1}{\mathrm{Pr}_s}\nabla^2 S = 0. \tag{2.9}$$

Without loss of generality, we choose $\partial_x T_0 = -1$, $\beta > 0$, and $\partial_z S_0 = -1$, and use the spectral method [12] to solve Eqs. (2.7)–(2.9): An $e^{\lambda t}$ dependence is assumed for all variables and we expand the spatial terms in Fourier-Chebychev series (Chebychev in x and Fourier in z). We make use of the following convolution relation [12]:

$$\widehat{(f\cdot g)}_k = \frac{1}{2}\left(\sum_{k=p+q}\hat{f}_p\cdot\hat{g}_q + \sum_{k=|p-q|}\hat{f}_p\cdot\hat{g}_q\right) \tag{2.10}$$

(where $\{\hat{f}_i\}$ and $\{\hat{g}_i\}$ are the expansion coefficients of $f(x)$ and $g(x)$ in the Chebychev spectral space) to write the product of two functions as a product of a square matrix with a vector in the Chebychev spectral space:

$$\begin{bmatrix} \widehat{fg}_0 \\ \cdot \\ \cdot \\ \cdot \\ \cdot \\ \widehat{fg}_n \end{bmatrix} = \mathbf{F}\cdot\begin{bmatrix} \hat{g}_0 \\ \cdot \\ \cdot \\ \cdot \\ \cdot \\ \hat{g}_n \end{bmatrix}, \tag{2.11}$$

where $\mathbf{F}$ is a square matrix whose elements are linear combinations of the $\{\hat{f}_i\}$. [Note that Eq. (2.11) corrects the relation (3.1.28) in Ref. [12]]. Hence in Eqs. (2.7)–(2.9) the functions and derivative operators in front of the variables (ψ, T, and S) can be written as square matrixes in the spectral space, and a generalized eigenvalue equation is obtained,

$$\mathcal{M}\cdot\mathbf{V} = \lambda\mathcal{L}\cdot\mathbf{V}, \tag{2.12}$$

where $\mathcal{M}$ and $\mathcal{L}$ are matrixes obtained from Eqs. (2.7)–(2.9). The vector $\mathbf{V} = (\psi, T, S)$ and the matrix $\mathcal{M}$ are functions of the set of control parameters $(\mathrm{Gr}, \mathrm{Gr}_s/\mathrm{Gr}, \mathrm{Pr}, \mathrm{Pr}_s)$ [or, alternatively, $(\mathrm{Ra}, \mathrm{Ra}_s, \mathrm{Pr}, \mathrm{Pr}_s)$]. Boundary conditions $\psi = \partial_x\psi = T = \partial_x S_0 = 0|_{x=\pm 1}$ are incorporated into Eq. (2.12) using the tau approximation [12]. Analytically one can show that the system is always stable to zero vertical wave number perturbations. For nonzero vertical wave numbers, we numerically solve this equation (with the solver from the LAPACK package) in the parameter space to find neutral stability curves. Our numerical solutions exhibit good resolution when we increase the number of modes (i.e., the spectrum shows power-law decay and remains flat at the higher mode number

end of the spectrum). In our calculation we fix the Prandtl number Pr=7 (for water at room temperature) and vary the solute Prandtl number Pr_s from 7×10^1 to 7×10^6. For $|\mathrm{Ra}_s|\geqslant O(10^3)$ the convergence is satisfactory when we use as few as 32 modes for all solute Prandtl numbers in the range $\{7\times10^1\leqslant\mathrm{Pr}_s\leqslant7\times10^6\}$. For $|\mathrm{Ra}_s|<O(10^3)$ we need to increase the number of modes to 48 to obtain good convergence for solute Prandtl numbers $\mathrm{Pr}_s=7\times10^1$, 7×10^2, and 7×10^3.

B. Weakly nonlinear analysis

The method of normal forms [13] is used to investigate the behavior of finite amplitude solutions in the neighborhood of critical points obtained from the linear theory. We rewrite Eqs. (2.1)–(2.3) in the following general form:

$$(\partial_t\mathcal{L}-\mathcal{M})\mathbf{V}=\mathbf{N}(\mathbf{V},\mathbf{V}), \tag{2.13}$$

where $\mathbf{V}=(\psi,T,S)$ and $\mathcal{M}$ and $\mathcal{L}$ are the same as in Eq. (2.12); $\mathbf{N}$ is the nonlinear term on the right-hand side of Eqs. (2.1)–(2.3), defined explicitly as follows:

$$\mathbf{N}(\mathbf{V}_1,\mathbf{V}_2)\equiv\begin{pmatrix} J(\psi_1,\nabla^2\psi_2)\\ J(\psi_1,T_2)\\ J(\psi_1,S_2)\end{pmatrix}. \tag{2.14}$$

The matrix $\mathcal{M}$ is intrinsically complex and non-Hermitian in our system. In the case of stationary bifurcations, we use $A(t)$ for the amplitude of the e^{ikz} mode and its complex conjugate $A^*(t)$ for the e^{-ikz} mode. In the case of Hopf bifurcations, we use $A(t)$ for the amplitude of the $e^{i(kz+\omega t)}$ mode and $B(t)$ for the $e^{i(kz-\omega t)}$ mode. Because $\mathcal{M}$ is complex and non-Hermitian, $B(t)$ is not complex conjugate to $A(t)$ and we have to treat these two amplitudes separately.

1. Stationary bifurcations

From [13,14], we write

$$\mathbf{V}=\sum_{k=1}^{\infty}\mathbf{V}_k,\quad \mathbf{V}_k=\sum_{l=0}^{k}\mathbf{V}_k^l A^{k-l}A^{*l}, \tag{2.15}$$

$$\mathbf{N}=\sum_{k=2}^{\infty}\mathbf{N}_k,\quad \mathbf{N}_k=\sum_{l=0}^{k}\mathbf{N}_k^l A^{k-l}A^{*l}, \tag{2.16}$$

$$\dot{A}=g(A,A^*)=\sum_{k=1}^{\infty}g_k(A,A^*),$$

$$g_k(A,A^*)=\sum_{l=0}^{l=k}g_k^l A^{k-l}A^{*l}. \tag{2.17}$$

With $\partial_t=\dot{A}\partial_A+\dot{A}^*\partial_{A^*}$, we determine $\dot{A}=g(A,A^*)$ and $\mathbf{V}$ simultaneously to the third order. To first order, we obtain

$$g_1^1=0, \tag{2.18}$$

$$(g_1^0\mathcal{L}-\mathcal{M})\mathbf{V}_1^0=\mathbf{0}, \tag{2.19}$$

$$(g_1^0\mathcal{L}-\mathcal{M})\mathbf{V}_1^1=\mathbf{0}. \tag{2.20}$$

Equations (2.19) and (2.20) are the eigenvalue equations in the linear theory, i.e., Eqs. (2.7)–(2.9) plus the complex conjugates of these three equations. To second order, we have

$$g_2^0=g_2^1=g_2^2=0, \tag{2.21}$$

$$(2g_1^0\mathcal{L}-\mathcal{M})\mathbf{V}_2^0=\mathbf{N}_2^0=\mathbf{N}(\mathbf{V}_1^0,\mathbf{V}_1^0), \tag{2.22}$$

$$(2g_1^0\mathcal{L}-\mathcal{M})\mathbf{V}_2^1=\mathbf{N}_2^1=\mathbf{N}(\mathbf{V}_1^1,\mathbf{V}_1^0)+\mathbf{N}(\mathbf{V}_1^0,\mathbf{V}_1^1), \tag{2.23}$$

$$(2g_1^0\mathcal{L}-\mathcal{M})\mathbf{V}_2^2=\mathbf{N}_2^2=\mathbf{N}(\mathbf{V}_1^1,\mathbf{V}_1^1). \tag{2.24}$$

To the third order, we have

$$g_3^0=g_3^2=g_3^3=0, \tag{2.25}$$

$$(3g_1^0\mathcal{L}-\mathcal{M})\mathbf{V}_3^0=\mathbf{N}_3^0=\mathbf{N}(\mathbf{V}_2^0,\mathbf{V}_1^0)+\mathbf{N}(\mathbf{V}_1^0,\mathbf{V}_2^0), \tag{2.26}$$

$$(3g_1^0\mathcal{L}-\mathcal{M})\mathbf{V}_3^1+g_3^1\mathcal{L}\mathbf{V}_1^0=\mathbf{N}_3^1, \tag{2.27}$$

plus the complex conjugates of Eqs. (2.26) and (2.27). At the stationary bifurcation points, $g_1^0=0$ and from the solvability condition of Eq. (2.27) we can determine g_3^1 by demanding the projection of Eq. (2.27) along the eigenvector $\mathbf{V}_1^0$ to vanish. We take the inner product of Eq. (2.27) with the vector $\mathbf{Y}$ [which is an eigenvector of the adjoint operator of $(g_1^0\mathcal{L}-\mathcal{M})$: $(g_1^0\mathcal{L}-\mathcal{M})_{\mathrm{ad}}\cdot\mathbf{Y}=-\mathcal{M}\mathbf{Y}=\mathbf{0}$ at the critical points] and the sum of the inner products should be zero; thus we obtain g_3^1 as

$$g_3^1=\frac{\langle\mathbf{Y},\mathbf{N}_3^1\rangle}{\langle\mathbf{Y},\mathcal{L}\mathbf{V}_1^0\rangle}, \tag{2.28}$$

where $\mathbf{N}_3^1=\mathbf{N}(\mathbf{V}_2^0,\mathbf{V}_1^1)+\mathbf{N}(\mathbf{V}_2^1,\mathbf{V}_1^0)+\mathbf{N}(\mathbf{V}_1^1,\mathbf{V}_2^0)+\mathbf{N}(\mathbf{V}_1^0,\mathbf{V}_2^1)$, and the notation $\langle\ ,\ \rangle$ refers to the inner product operations. The amplitude equation for $A(t)$ is then the complex Ginzburg-Landau equation,

$$\dot{A}=g_1^0A+g_3^1A|A|^2, \tag{2.29}$$

where we have dropped all higher-order $[O(|A|^5)]$ terms. For stationary bifurcations, g_1^0 is real in the neighborhood of the critical points. If the real part of $g_3^1[\mathrm{Re}(g_3^1)]$ is negative, the bifurcation is supercritical, equilibrium solutions exist and are stable; if $\mathrm{Re}(g_3^1)$ is positive, the bifurcation is subcritical, and equilibrium solutions exist for $g_1^0<0$ and are unstable.

2. Hopf bifurcations

As mentioned before, $\mathcal{M}$ is a general complex, non-Hermitian matrix and we have two independent amplitudes $A(t)$ (modes with $e^{i(\omega t+kz)}$ dependence) and $B(t)$ (modes with $e^{i(-\omega t+kz)}$ dependence) plus the complex conjugates $A^*(t)[\equiv D(t)]$ and $B^*(t)[\equiv C(t)]$. Thus, in this case we have

$$\mathbf{V}=\sum_{k=1}^{\infty}\mathbf{V}_k,\quad \mathbf{V}_k=\sum_{a+b+c+d=k}\mathbf{V}^{abcd}A^aB^bC^cD^d, \tag{2.30}$$

$$\mathbf{N}=\sum_{k=2}^{\infty}\mathbf{N}_k, \quad \mathbf{N}_k=\sum_{a+b+c+d=k}\mathbf{N}^{abcd}A^aB^bC^cD^d, \tag{2.31}$$

$$\dot{A}=g(A,B,C,D)=\sum g^{abcd}A^aB^bC^cD^d, \tag{2.32}$$

$$\dot{B}=f(A,B,C,D)=\sum f^{abcd}A^aB^bC^cD^d. \tag{2.33}$$

As a simple illustration of the notation:

$$\mathbf{N}^{2001}\equiv\mathbf{N}(\mathbf{V}^{2000},\mathbf{V}^{0001})+\mathbf{N}(\mathbf{V}^{1001},\mathbf{V}^{1000}) +\mathbf{N}(\mathbf{V}^{0001},\mathbf{V}^{2000})+\mathbf{N}(\mathbf{V}^{1000},\mathbf{V}^{1001}),$$

where $\mathbf{V}^{2000}$ and $\mathbf{V}^{1001}$ are obtained from the second order equations in the expansion. $\mathbf{V}^{1000}$ is the eigenfunction from linear stability analysis with $e^{i\omega t}$ dependence, $\mathbf{V}^{0100}$ is the eigenfunction with $e^{-i\omega t}$ dependence; $\mathbf{V}^{0001}$ is the complex conjugate of $\mathbf{V}^{1000}$, and $\mathbf{V}^{0010}$ is the complex conjugate of $\mathbf{V}^{0100}$. Following the procedures in the previous subsection, we obtain the amplitude equations for $A(t)$ and $B(t)$:

$$\dot{A}=(\epsilon+i\omega)A+\alpha_1A|A|^2+\alpha_2A|B|^2, \tag{2.34}$$

$$\dot{B}=(\epsilon-i\omega)B+\beta_1B|B|^2+\beta_2B|A|^2, \tag{2.35}$$

where ϵ (a small real number) is the growth rate ($\epsilon=0$ at criticality, $\epsilon<0$ at subcriticality, and $\epsilon>0$ at supercriticality) and α's and β's are given as follows from the solvability conditions [$\mathbf{Y}_a$ and $\mathbf{Y}_b$, respectively, satisfy $(i\omega\mathcal{L}-\mathcal{M})_{\rm ad}\mathbf{Y}_a=0$ and $(-i\omega\mathcal{L}-\mathcal{M})_{\rm ad}\mathbf{Y}_b=0$, both $\mathbf{Y}_a$ and $\mathbf{Y}_b$ have e^{-ikz} dependence]:

$$\alpha_1=\frac{\langle\mathbf{Y}_a,\mathbf{N}^{2001}\rangle}{\langle\mathbf{Y}_a,\mathcal{L}\mathbf{V}^{1000}\rangle}, \quad \alpha_2=\frac{\langle\mathbf{Y}_a,\mathbf{N}^{1110}\rangle}{\langle\mathbf{Y}_a,\mathcal{L}\mathbf{V}^{1000}\rangle}, \tag{2.36}$$

$$\beta_1=\frac{\langle\mathbf{Y}_b,\mathbf{N}^{0210}\rangle}{\langle\mathbf{Y}_b,\mathcal{L}\mathbf{V}^{0100}\rangle}, \quad \beta_2=\frac{\langle\mathbf{Y}_b,\mathbf{N}^{1101}\rangle}{\langle\mathbf{Y}_b,\mathcal{L}\mathbf{V}^{0100}\rangle}. \tag{2.37}$$

Equations (2.34)–(2.35) are the same as the complex coupled Ginzburg-Landau (CCGL) equations derived in [15] for a binary fluid, and are the spatially uniform CCGL equations in [16] for the nonresonant cases in the thermally coupled two layer problem. Although in this case the two amplitudes are strongly temporally coupled (see [17] and [18] and references therein) the spatial symmetry in our system has reduced all the additional coupling terms to zero and the form of the CCGL is a reflection of the symmetry in the system [15].

C. Analysis of the coupled amplitude equations

Writing $A(t)=\rho_a(t)e^{i\theta_a(t)}$ and $B(t)=\rho_b(t)e^{i\theta_b(t)}$, where $\rho_a(t)$, $\theta_a(t)$ and $\rho_b(t)$, $\theta_b(t)$ are all real functions, Eqs. (2.34) and (2.35) give us

$$\dot{\rho}_a=\epsilon\rho_a+\mathrm{Re}(\alpha_1)\rho_a^3+\mathrm{Re}(\alpha_2)\rho_a\rho_b^2, \tag{2.38}$$

$$\dot{\theta}_a=\omega+\mathrm{Im}(\alpha_1)\rho_a^2+\mathrm{Im}(\alpha_2)\rho_b^2, \tag{2.39}$$

$$\dot{\rho}_b=\epsilon\rho_b+\mathrm{Re}(\beta_1)\rho_b^3+\mathrm{Re}(\beta_2)\rho_b\rho_a^2, \tag{2.40}$$

$$\dot{\theta}_b=-\omega+\mathrm{Im}(\beta_1)\rho_b^2+\mathrm{Im}(\beta_2)\rho_a^2, \tag{2.41}$$

where $\mathrm{Re}(\alpha)$ is the real part and $\mathrm{Im}(\alpha)$ is the imaginary part of α. The square of the amplitudes of the asymptotic equilibrium state, depending on the values of the coefficients in Eqs. (2.38) and (2.40), can be any one of the following four combinations:

$$|\rho_{a0}|^2=-\epsilon\frac{-\mathrm{Re}(\alpha_2)+\mathrm{Re}(\beta_1)}{\mathrm{Re}(\alpha_1)\mathrm{Re}(\beta_1)-\mathrm{Re}(\alpha_2)\mathrm{Re}(\beta_2)}\equiv-\gamma_a\epsilon, \tag{2.42}$$

$$|\rho_{b0}|^2=-\epsilon\frac{-\mathrm{Re}(\beta_2)+\mathrm{Re}(\alpha_1)}{\mathrm{Re}(\alpha_1)\mathrm{Re}(\beta_1)-\mathrm{Re}(\alpha_2)\mathrm{Re}(\beta_2)}\equiv-\gamma_b\epsilon,$$

$$|\rho_{a0}|^2=-\frac{\epsilon}{\mathrm{Re}(\alpha_1)}, \quad |\rho_{b0}|^2=0, \tag{2.43}$$

$$|\rho_{a0}|^2=0, \quad |\rho_{b0}|^2=-\frac{\epsilon}{\mathrm{Re}(\beta_1)}, \tag{2.44}$$

$$|\rho_{a0}|^2=0, \quad |\rho_{b0}|^2=0. \tag{2.45}$$

The standing wave solution in Eq. (2.42) exists only if γ_a and γ_b are of the same sign. If γ_a and γ_b are both negative, the bifurcations are supercritical, and oscillatory solutions exist for $\epsilon>0$. If γ_a and γ_b are both positive, the bifurcations are subcritical, and oscillatory solutions exist for $\epsilon<0$. If $\mathrm{Re}(\alpha_1)$ and $\mathrm{Re}(\beta_1)$ are both negative (positive), then the two supercritical (subcritical) traveling waves with amplitudes given by Eqs. (2.43)–(2.44) coexist for $\epsilon>0$ ($\epsilon<0$). If $\mathrm{Re}(\alpha_1)$ and $\mathrm{Re}(\beta_1)$ are of opposite signs, subcritical traveling waves exist and the amplitudes are given by Eq. (2.43) for $\mathrm{Re}(\alpha_1)>0$ or Eq. (2.44) for $\mathrm{Re}(\beta_1)>0$. As we vary ϵ from negative to positive values, the amplitudes of the asymptotic equilibrium state change from the asymptotic amplitudes in Eq. (2.43) for $\mathrm{Re}(\alpha_1)>0$ [Eq. (2.44) for $\mathrm{Re}(\beta_1)>0$] to those in Eq. (2.44) [Eq. (2.43)]. The stability analysis for the equilibrium states is straightforward: we write $\rho_a=\rho_{a0}+\delta\rho_a$ and $\rho_b=\rho_{b0}+\delta_{\rho b}$, where ρ_{a0} and ρ_{b0} are the equilibrium amplitudes, and substitute these expressions into Eqs. (2.38) and (2.40). To first order in $\delta_{\rho a}$ and $\delta_{\rho b}$ we obtain

$$\delta\dot{\rho}_a=[\epsilon+3\,\mathrm{Re}(\alpha_1)\rho_{a0}^2+\mathrm{Re}(\alpha_2)\rho_{b0}^2]\delta\rho_a +2\,\mathrm{Re}(\alpha_2)\rho_{a0}\rho_{b0}\delta\rho_b, \tag{2.46}$$

$$\delta\dot{\rho}_b=[\epsilon+3\,\mathrm{Re}(\beta_1)\rho_{b0}^2+\mathrm{Re}(\beta_2)\rho_{a0}^2]\delta\rho_b +2\,\mathrm{Re}(\beta_2)\rho_{a0}\rho_{b0}\delta\rho_a. \tag{2.47}$$

Assuming $e^{\lambda t}$ dependence for both $\delta\rho_a$ and $\delta\rho_b$, the stability analysis for the equilibrium state then boils down to solving the following eigenvalue equation:

$$\left(\begin{bmatrix} \epsilon + 3\mathrm{Re}\ (\alpha_1)\rho_{a0}^2 + \mathrm{Re}(\alpha_2)\rho_{b0}^2 & 2\,\mathrm{Re}(\alpha_2)\rho_{a0}\rho_{b0} \\ 2\,\mathrm{Re}(\beta_2)\rho_{a0}\rho_{b0} & \epsilon + 3\,\mathrm{Re}(\beta_1)\rho_{b0}^2 + \mathrm{Re}(\beta_2)\rho_{a0}^2 \end{bmatrix} - \lambda \mathbf{I} \right) \cdot \begin{bmatrix} \delta\rho_a \\ \delta\rho_b \end{bmatrix} = 0. \tag{2.48}$$

The equilibrium state is a stable fixed point (SF) if the real parts of the two eigenvalues are both negative; if the real parts are both positive, the equilibrium state is unstable (UN); the equilibrium is a saddle point (SP) if the real parts of the two eigenvalues are of opposite signs. We note that if either one of ρ_{a0} and ρ_{b0} is zero, the matrix in Eq. (2.48) is diagonal and the eigenvalues are real. For $\rho_{a0}^2=\rho_{b0}^2=0$, the two eigenvalues are $\lambda_1=\lambda_2=\epsilon$; for $\rho_{a0}^2=0$ and $\rho_{b0}^2=-\epsilon/\mathrm{Re}(\beta_1)$, the two eigenvalues are $\lambda_1=\epsilon[1-\mathrm{Re}(\alpha_2)/\mathrm{Re}(\beta_1)]$, $\lambda_2=-2\epsilon$; for $\rho_{a0}^2=-\epsilon/\mathrm{Re}(\alpha_1)$ and $\rho_{b0}^2=0$, the two eigenvalues are $\lambda_1=-2\epsilon$, $\lambda_2=\epsilon[1-\mathrm{Re}(\beta_2)/\mathrm{Re}(\alpha_1)]$. For a more complete analysis on the coupled amplitude equations, we refer the readers to [18].

III. RESULTS

In this section we summarize the results of our analyses. We identify two principal regimes (case I and case II), which differ in the nature of the unperturbed equilibrium. In case I (the double-diffusively-driven regime), the stratification ratio is large $[\beta\Delta S/\alpha\Delta T=\mathrm{Gr}_s/\mathrm{Gr}\geqslant O(1)]$ and the unperturbed equilibrium is a static state in the interior with thin boundary layers sustaining the zero solute flux at the walls. In case II (the shear-induced regime), the stratification ratio is small $[\beta\Delta S/\alpha\Delta T=\mathrm{Gr}_s/\mathrm{Gr}\ll O(1)]$ and the unperturbed equilibrium is a steady shear flow throughout the slot.

A. Double-diffusively-driven instability: $\beta\Delta S/\alpha\Delta T=\mathrm{Gr}_s/\mathrm{Gr}\geqslant O(1)$

In Fig. 2(a) we show the critical Rayleigh numbers ($\mathrm{Ra}_c\equiv g\alpha\Delta T_c d^3/\nu\kappa_t=\mathrm{Gr}_c\times\mathrm{Pr}$) versus the solute Rayleigh numbers ($|\mathrm{Ra}_s|\equiv g\beta|\partial_z S_0|d^4/\nu\kappa_s=\mathrm{Gr}_s\times\mathrm{Pr}_s$) for six different values of the diffusivity ratio $H(\equiv\mathrm{Pr}_s/\mathrm{Pr}=\kappa_t/\kappa_s)$. In this regime, results from our numerical calculations show that bifurcations are stationary, and the computed neutral curves are in satisfactory agreement with results presented in [5,7]. We also plot the critical wave number ($2k_c$) as a function of $|\mathrm{Ra}_s|$, and as shown in Fig. 2(b), our results are in good agreement with the asymptotic approximation [1,3,5] for $|\mathrm{Ra}_s|\geqslant 10^5$.

In our computation, we find that the bifurcations are all subcritical for $H\geqslant 10^3$ in this doubly diffusive solute Rayleigh number regime. Exceptions to Hart's conclusion [5] are found for $H=10$ and $H=10^2$, as shown in Fig. 3(a): Hart [5] concluded bifurcations are subcritical if $H>(-\mathrm{Ra}_s)^{1/6}$ and supercritical if $H<(-\mathrm{Ra}_s)^{1/6}$. In contrast, we find that for $H=10$ there are subcritical bifurcations for $H<(-\mathrm{Ra}_s)^{1/6}$, and for $H=10^2$ there are supercritical bifurcations for $H>(-\mathrm{Ra}_s)^{1/6}$. We propose a possible explanation for the different variation of g_3^1 as a function of $|\mathrm{Ra}_s|$ for different diffusivity ratio H in Fig. 3(b), where we plot the critical wave number ($2k_c$) as a function of solute Rayleigh number on the $|\mathrm{Ra}_s|$-$2k$ plane. (Note that from our definition of $|\mathrm{Ra}_s|$ this curve on the $|\mathrm{Ra}_s|$-$2k$ plane is the same for all diffusivity ratios $H>1$ in this regime of $|\mathrm{Ra}_s|$.) Dotted lines and dashed lines on the plane are the hypothetical dividing lines separating supercritical bifurcations ($g_3^1<0$ above the dividing line in our case) from subcritical bifurcations ($g_3^1>0$ below the dividing line in our case) as in Fig. 3 in [5]. For $H=10$ the hypothetical dividing line intersects the solid curve near $(|\mathrm{Ra}_s|,2k_c)\sim(10^7,20)$ and $\mathrm{Re}(g_3^1)$ drops from positive to negative values as $|\mathrm{Ra}_s|$ increases. The dividing

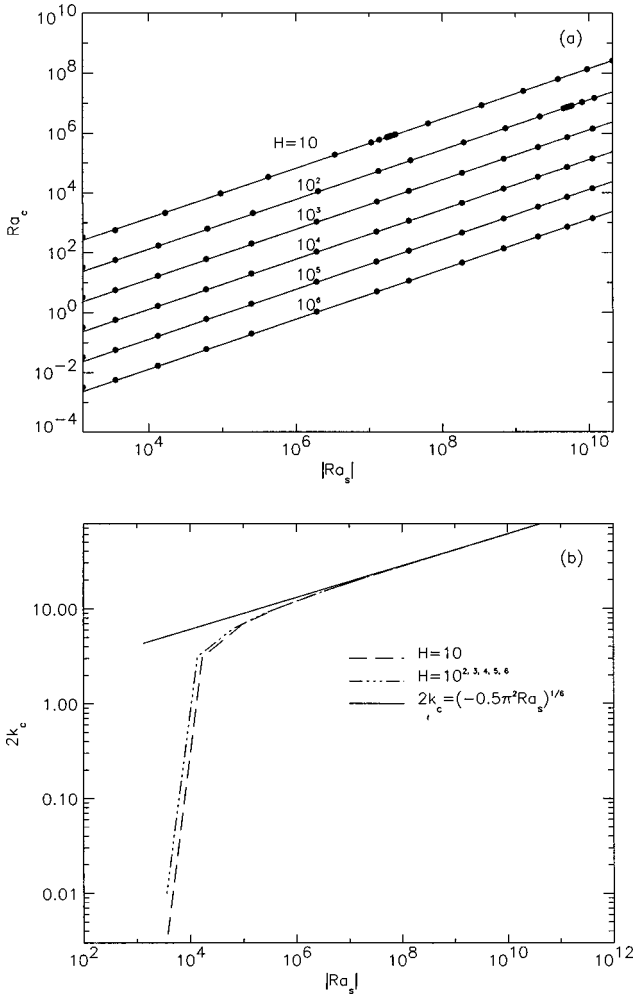

FIG. 2. Panel (a) Neutral curve for six values of the diffusivity ratio $H(=\kappa_t/\kappa_s)$ in the doubly diffusive instability (case I) regime $[\beta\Delta S/\alpha\Delta T\geqslant O(1)]$. The solid dots are from our calculations; the solid lines are the analytical results from [5]: $\mathrm{Ra}=2^{1/6}6^{1/2}|\mathrm{Ra}_s|^{5/6}(\pi)^{2/3}/(H-1)$. Thus, the solid lines are *not* fits to our computed results. In this regime the critical points are all stationary. We note that as far as the critical thermal Rayleigh numbers are concerned, the asymptotic approximation works quite well even for solute Rayleigh number $|\mathrm{Ra}_s|$ as small as 10^3. Panel (b) Critical wave number ($=2k_c$; we scale distances by $d/2$) vs solute Rayleigh number for the same cases displayed in panel (a). The analytical result from [5] deviates significantly from our computed results as $|\mathrm{Ra}_s|$ decreases below $\sim 10^5$.

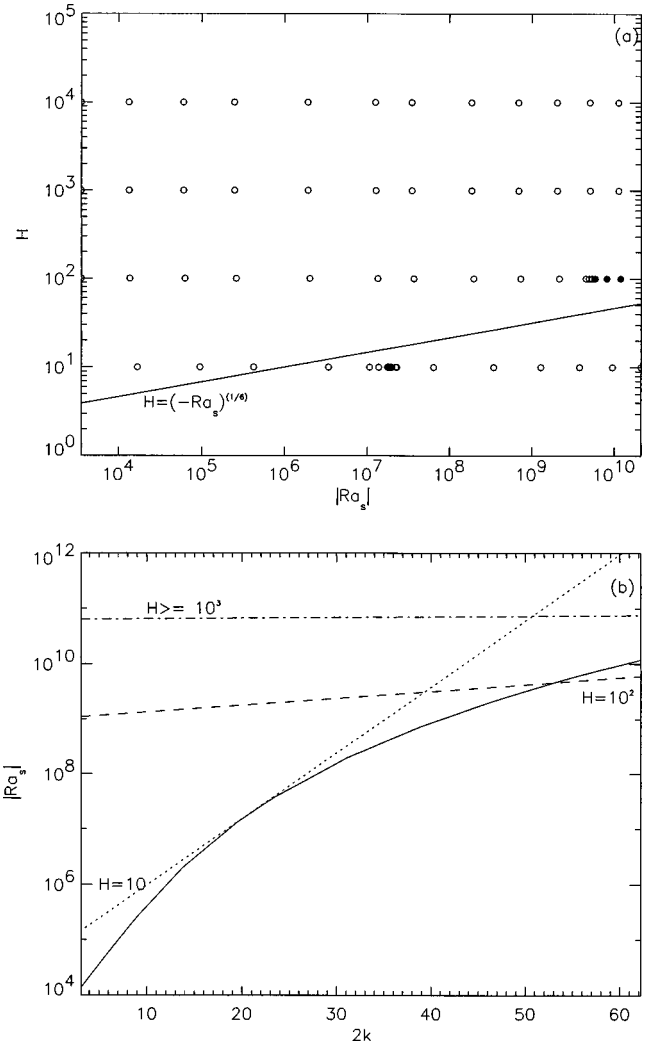

FIG. 3. Real part of the coefficient g_3^1 in Eq. (2.29) as a function of solute Rayleigh number for various values of diffusivity ratio H in the double diffusively driven regime. Panel (a) $\mathrm{Re}(g_3^1)$ for $H=10$, 10^2, 10^3 and 10^4. Open circles are for positive $\mathrm{Re}(g_3^1)$ (subcritical bifurcation), and solid circles are for negative $\mathrm{Re}(g_3^1$ (supercritical bifurcation). The solid line is $H=(-\mathrm{Ra}_s)^{1/6}$, above which bifurcations are subcritical, and below which bifurcations are supercritical [5]. Panel (b) Explanatory diagram for $\mathrm{Re}(g_3^1)$ as a function of $|\mathrm{Ra}_s|$ for different diffusivity ratios. The solid line is the critical wave number for given solute Rayleigh numbers on the $|\mathrm{Ra}_s|$-$2k$ plane for all diffusivity ratios in the double-diffusively-driven regime. The dotted line is the hypothetical dividing line for $H=10$, the dashed line is for $H=10^2$ and the dash-dotted line is for $H=10^3$. In accordance with [5], the range in the $|\mathrm{Ra}_s|$-$2k$ plane over which the finite amplitude instability is possible increases as H increases.

line intersects the curve again at $|\mathrm{Ra}_s|$ slightly greater than 10^7 and $\mathrm{Re}(g_3^1)$ jumps discontinuously to positive values. This then explains the variation of $\mathrm{Re}(g_3^1)$ as a function of $|\mathrm{Ra}_s|$ for $H=10$ near $|\mathrm{Ra}_s|=10^7$. For $H=10^2$, the dividing line may intersect the solid curve at $|\mathrm{Ra}_s|\sim 3\times 10^9$ and that is why the discontinuity occurs near $|\mathrm{Ra}_s|=3\times 10^9$ for $H=10^2$. For higher diffusivity ratios, the hypothetical dividing line may not intersect the solid curve for $10^4\leqslant|\mathrm{Ra}_s|\leqslant 10^{10}$ and thus there is no supercritical bifurcation and all bifurcations are subcritical in this double-diffusively-driven regime.

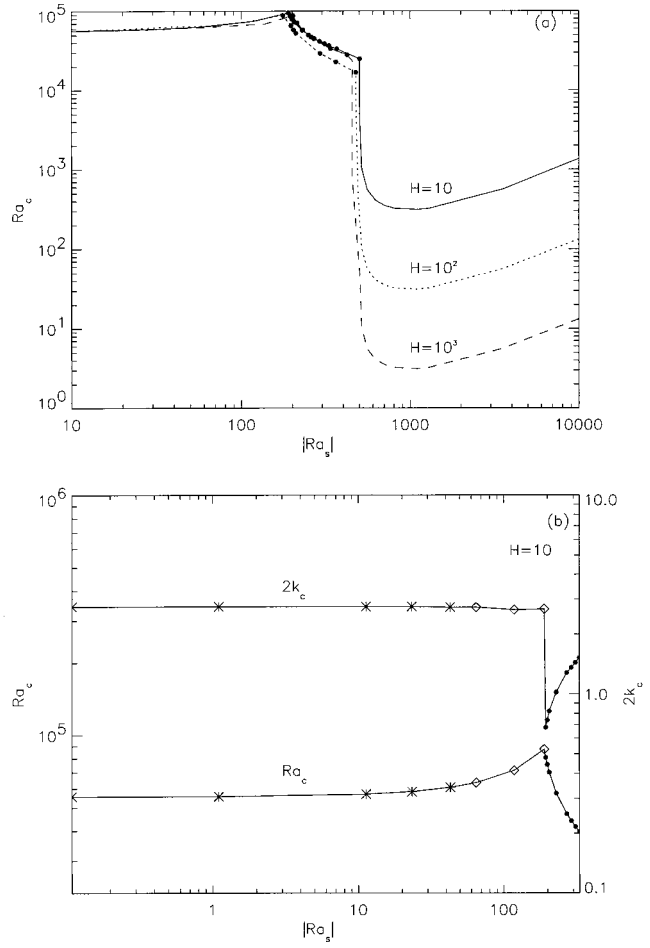

FIG. 4. Critical curves in the shear-induced regime; 97 modes are used for these calculations. Panel (a) Critical thermal Rayleigh numbers Ra_c as functions of solute Rayleigh number $|\mathrm{Ra}_s|$ for $H=10$, 10^2, and 10^3 in the transition regime; Pr=7 (for water). On each curve, solid dots indicate the Hopf bifurcation cases for which the coefficients in the amplitude equations are calculated. Panel (b) Critical curves for $H=10$, Pr=7 in the shear-induced regime. The left vertical axis is the critical thermal Rayleigh number Ra_c; the right y axis is the critical wave number $2k_c$. The solid lines represent stationary instability, while the dashed lines represent overstability. The diamonds placed on the solid lines indicate subcritical bifurcations; asterisks indicate supercritical bifurcations; solid dots (on the dashed lines) indicate points where the coefficients in the amplitude equations are calculated (the secondary stability is listed in Table I). As $|\mathrm{Ra}_s|$ decreases below 10^4, Ra_c reaches minimum at $|\mathrm{Ra}_s|=10^3$. (For $H=10^2$, the salty water case, the minimum is $\mathrm{Ra}_c=31$, as in [7].) Careful investigation near $|\mathrm{Ra}_s|=10^3$ shows that the stationary branch remains the lowest branch until $|\mathrm{Ra}_s|$ decreases below 500, at which point the overstable branch becomes the most unstable branch. We further note that the transition from overstability to stationary instability occurs at $|\mathrm{Ra}_s|\sim 200$, and the threshold solute Rayleigh number (defined in Sec. IV) $|\mathrm{Ra}_{s,\mathrm{th}}|\sim 50$.

B. Shear-induced instability: $\beta\Delta S/\alpha\Delta T=\mathrm{Gr}_s/\mathrm{Gr}\ll O(1)$

Here we present results of calculations for three diffusivity ratios: $H=\kappa_t/\kappa_s=10$, 10^2, and 10^3 (Figs. 4 and 5). In the thermohaline slot convection case, the critical thermal Rayleigh number and the critical wave number for solute Rayleigh number $10^2\leqslant|\mathrm{Ra}_s|\leqslant 10^3$ in our computation [Fig. 4(a)]

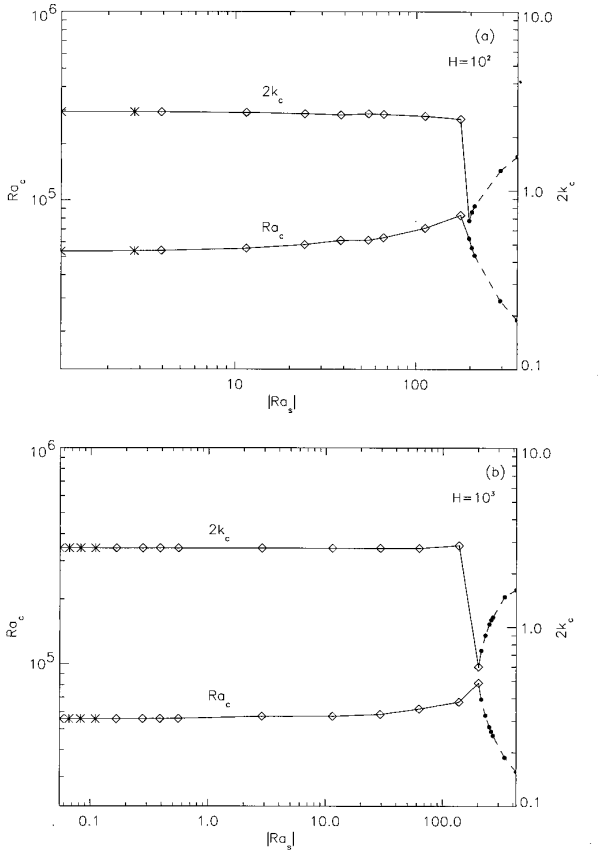

FIG. 5. Panel (a): Critical curves for salty water ($H=10^2$, Pr $=7$) in the shear-driven regime. The left y axis is the critical thermal Rayleigh number Ra_c and the right y axis is the critical wave number $2k_c$. For $10^2 \leqslant |\mathrm{Ra}_s| \leqslant 10^3$ the critical thermal Rayleigh number increases less steeply than in [7] and reaches a local maximum near $|\mathrm{Ra}_s|=10^2$; asymptotically it reaches the value of 5.5×10^4, the critical thermal Rayleigh number in vertical slot convection [10]. The critical wave number decreases first as the solute Rayleigh number decreases from 10^3, reaches a local minimum at $|\mathrm{Ra}_s| \sim 10^2$, and climbs up to a local maximum, and then asymptotically reaches the value of 2×1.38, the critical wave number in vertical slot convection [10]. The transition from overstable instability to stationary instability occurs around $|\mathrm{Ra}_s| \sim 200$, and the threshold solute Rayleigh number $|\mathrm{Ra}_{s,\mathrm{th}}| \sim 3.5$. Panel (b): The corresponding curves for $H=10^3$, Pr$=7$. The transition from overstability to stationary instability occurs around $|\mathrm{Ra}_s| \sim 200$, and the threshold solute Rayleigh number $|\mathrm{Ra}_{s,\mathrm{th}}| \sim 0.08$.

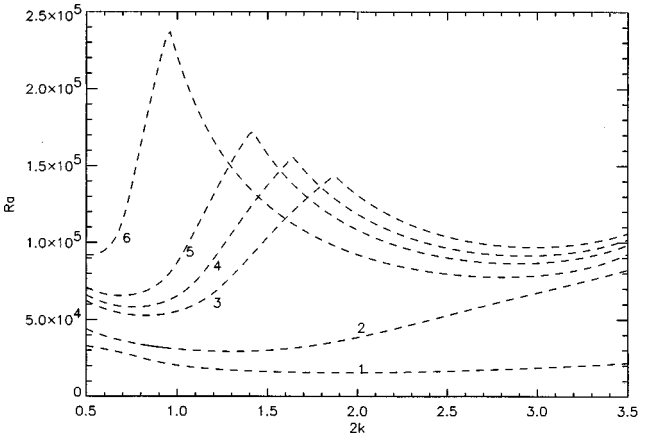

FIG. 6. Neutral curves for salty water ($H=10^2$, Pr$=7$) for a density stratification ratio in the range $2\times 10^{-5} \leqslant \mathrm{Gr}_s/\mathrm{Gr} = \beta\Delta S/\alpha\Delta T \leqslant 4\times 10^{-4}$. All instabilities are overstable (dashed lines). The density stratification ratio for curve 1 is $\beta\Delta S/\alpha\Delta T = 4\times 10-4$ and the solute Rayleigh number at critical point is $|\mathrm{Ra}_s| = 477.14$. Curve 2: $\beta\Delta S/\alpha\Delta T = 10^{-4}$, $|\mathrm{Ra}_s| = 292.45$. Curve 3: $\beta\Delta S/\alpha\Delta T = 4\times 10^{-5}$, $|\mathrm{Ra}_s| = 210.48$. Curve 4: $\beta\Delta S/\alpha\Delta T = 3.5\times 10^{-5}$, $|\mathrm{Ra}_s| = 203.44$. Curve 5: $\beta\Delta S/\alpha\Delta T = 3\times 10^{-5}$, $|\mathrm{Ra}_s| = 196.53$. Curve 6: $\beta\Delta S/\alpha\Delta T = 2\times 10^{-5}$, $|\mathrm{Ra}_s| = 155.03$. For curves 2, 3, and 4, we note that the minima at the larger wave number ($2k \sim 2.8$ for all three curves) have slightly larger critical thermal Rayleigh numbers than those at smaller wave numbers. It is likely that in [7] these minima are used instead, and thus have a constant critical wave number ~ 3 [7] in the corresponding range of solute Rayleigh numbers (in [7] this range is $2 < |R_s| < 5$.)

are different from those in [7] for the corresponding solute Rayleigh number $1 \leqslant |R_s| \leqslant 10$ (the solute Rayleigh number defined in [7] is $R_s \equiv g\beta\Delta d^3/\kappa_t \nu = \mathrm{Ra}_s/H$). We carefully checked both convergence and resolution in our numerics by increasing the number of modes, and found that the neutral curves using 64 modes are indistinguishable from those obtained with 48 modes for all three values of H everywhere except near $|\mathrm{Ra}_s| \sim 200$, where $\gtrsim 96$ modes are required. Thus we can rule out distortion of the neutral curves due to the lack of convergence or sufficient resolution [9]. (97 modes are used in all of our calculations in this regime.) The discrepancies for the salty water case may be understood as follows. In Fig. 6 we show the neutral curves for several density stratification ratios for $H=10^2$. In our calculations, we calculate the critical Grashof number Gr_c for a fixed stratification ratio $\mathrm{Gr}_s/\mathrm{Gr}$ and then calculate the solute Rayleigh number $|\mathrm{Ra}_s|$ on the neutral curve from $|\mathrm{Ra}_s| = \mathrm{Gr}_s/\mathrm{Gr} \times \mathrm{Gr}_c \times H$. The range of solute Rayleigh numbers at critical points for these curves is $155 \leqslant |\mathrm{Ra}_s| \leqslant 480$, and the corresponding range of solute Rayleigh number in [7] is $1.5 \leqslant R_s \leqslant 4.8$. For $\mathrm{Gr}_s/\mathrm{Gr} = 4\times 10^{-5}$, 3.5×10^{-5}, and 3.0×10^{-5} two local minima are found in the neutral curves. The critical wave numbers are, respectively, $2k_c = 0.82$, 0.76, and 0.68. The other minima for these three curves occur at the wave number $2k_c = 2.92$, which is the same as the critical wave number in [7] for the corresponding solute Rayleigh numbers. Thus it is likely that in [7] the local minima at larger vertical wave numbers was used instead, leading to different results from ours in this particular range of solute Rayleigh number for the thermohaline slot convection.

Table I summarizes the secondary stabilities for the solid points on the oscillatory bifurcation branches of the critical curves in Figs. 4(b) and 5 (dashed lines). For fixed $|\mathrm{Ra}_s|$ in the range of $\sim 10^3$, the neutral curves on the Ra-k plane are very flat near the critical points ([7], and references therein) for all diffusivity ratios in our calculations, so that it is difficult to determine the critical wave number precisely from the calculations. Hence we did not calculate the coefficients in the amplitude equations for this range of Ra_s. In the next section we discuss why the critical wave numbers are not unique for $|\mathrm{Ra}_s| \sim 10^3$.

IV. SUMMARY AND DISCUSSIONS

The instabilities are categorized into two cases. Case I is the double-diffusively-driven regime [$\beta\Delta S/\alpha\Delta T \geqslant O(1)$],

TABLE I. Summary of the stabilities for marked points on the oscillatory branches of the critical curves in Figs. 4–6. For each solute Rayleigh number, the upper brace (''sub'' in the front) describes the stabilities or existence of the four fixed points for $\epsilon<0$ and the lower one (''sup'' in the front) is for $\epsilon>0$. In each brace, X means the fixed point does not exist, ''SF'' stands for stable fixed point, UN is for unstable, and SP is for saddle point. For example, sub (X, UN, SP, SF) means for $\epsilon<0$ (sub) the equilibrium state with amplitudes given in Eq. (2.42) does not exist (X), the state described in Eq. (2.43) is an unstable node (UN), the state with amplitudes in Eq. (2.44) is a saddle point (SP), and the trivial equilibrium state in Eq. (2.45) is a stable fixed point (SF).

$H=10$		$H=10^2$		$H=10^3$	
$\lvert Ra_s\rvert=330.137$	sub(X,SP,X,SF)	$\lvert Ra_s\rvert=362.817$	sub(UN,SP,SP,SF)		
	sup(X,X,SP,UN)		sup(X,X,X,UN)		
$\lvert Ra_s\rvert=310.725$	sub(X,UN,X,SF)	$\lvert Ra_s\rvert=292.451$	sub(UN,SP,SP,SF)	$\lvert Ra_s\rvert=383.746$	sub(X,UN,X,SF)
	sup(X,X,SF,UN)		sup(X,X,X,UN)		sup(X,X,SF,UN)
$\lvert Ra_s\rvert=290.863$	sub(X,UN,X,SP)	$\lvert Ra_s\rvert=210.425$	sub(UN,SP,SP,SF)	$\lvert Ra_s\rvert=296.400$	sub(X,UN,X,SF)
	sup(X,X,SP,UN)		sup(X,X,X,UN)		sup(X,X,SF,UN)
$\lvert Ra_s\rvert=270.592$	sub(X,UN,X,SF)	$\lvert Ra_s\rvert=203.444$	sub(UN,SP,SP,SF)	$\lvert Ra_s\rvert=220.579$	sub(UN,SP,X,SF)
	sup(X,X,SF,UN)		sup(X,X,X,UN)		sup(X,X,SF,UN)
$\lvert Ra_s\rvert=229.212$	sub(X,SP,X,SF)	$\lvert Ra_s\rvert=196.529$	sub(UN,SP,SP,SF)	$\lvert Ra_s\rvert=210.806$	sub(UN,SP,X,SF)
	sup(X,X,SP,UN)		sup(X,X,X,UN)		sup(X,X,SF,UN)
$\lvert Ra_s\rvert=205.215$	sub(X,UN,X,SF)			$\lvert Ra_s\rvert=200.988$	sub(X,UN,X,SF)
	sup(X,X,SF,UN)				sup(X,X,SF,UN)
$\lvert Ra_s\rvert=199.080$	sub(X,UN,X,SF)			$\lvert Ra_s\rvert=181.273$	sub(UN,SPX,SF)
	sup(X,X,SF,UN)				sup(X,X,SP,UN)
$\lvert Ra_s\rvert=194.311$	sub(X,UN,X,SF)				
	sup(X,X,SF,UN)				

where the unperturbed shear flow is significant only near the vertical boundaries. The virtually static, unperturbed equilibrium is sustained by the imposing solute stratification in both vertical and horizontal directions. For $H>1$ this equilibrium can become unstable due to doubly diffusive instabilities, even though it remains stable to perturbation in the $H\rightarrow 1$ limit [3,5]. Case II is the shear-induced regime [$\beta\Delta S/\alpha\Delta T \ll O(1)$], where the backgrond equilibrium is a shear flow throughout the slot. In the $H=1$ limit the system reduces to the vertical slot convection and the shear flow loses stability when the thermal Rayleigh number exceeds the critical value $Ra_c=5.5\times 10^4$. For diffusivity ratio $H>1$ the critical thermal Rayleigh number Ra_c depends on the value of $\lvert Ra_s\rvert$. Ra_c is independent of H for $\lvert Ra_s\rvert$ smaller than 10^2, because the solute has no effect on the instability. For $\lvert Ra_s\rvert\geqslant 10^2$ the stabilizing vertical solute gradient has significantly decreased the amplitude of the shear flow [Fig. 7(b)], hence Ra_c depends on H and the instability is replaced by overstable instability. From Figs. 4 and 5 we find that as the solute Rayleigh number $\lvert Ra_s\rvert$ decreases below 10, both the critical thermal Rayleigh number and the critical wave number asymptotically approach those in the vertical slot convection, where $Ra_c=5.5\times 10^4$ and $k_c=1.38$ [2,9]. Though the critical states are all stationary at $\lvert Ra_s\rvert\sim 10$ for the three diffusivity ratios in Figs. 4 and 5, the bifurcation remains supercritical for $H=10$ and turns subcritical for $H=10^2$ and $H=10^3$. For zero solute Rayleigh number (vertical slot convection) the critical state is stationary and supercritical [2]. As the solute Rayleigh number increases above zero, the critical state changes from supercritical stationary bifurcation to subcritical stationary bifurcation at some solute Rayleigh number (we define this value as the threshold solute Rayleigh number $Ra_{s,th}$). From Figs. 4 and 5, $\lvert Ra_{s,th}\rvert\sim 50$ for $H=10$, $\lvert Ra_{s,th}\rvert\sim 3.5$ for $H=10^2$ and $\lvert Ra_{s,th}\rvert\sim 0.1$ for $H=10^3$. The effect of different diffusivities is well illustrated by the dependence of the threshold solute Rayleigh number on the diffusivity ratio. For large solute diffusivities ($H\rightarrow 1$), the solute stratification ($\lvert Ra_s\rvert$) must be large enough to change the characteristics of the instability because the solute diffuses almost as efficiently as heat, while for small solute diffusivities ($H>1$), a comparatively smaller solute stratification (smaller $\lvert Ra_s\rvert$) is enough to change the bifurcation to subcritical because the solute diffuses much less efficiently than heat [10]. Hence, the smaller the solute diffusivity, the smaller the threshold solute Rayleigh number. The transition from supercritical stationary to subcritical stationary bifurcation suggests that we should go to a higher order to investigate the finite-amplitude stability and the possibility for steady state equilibrium [13,10].

We now explain why there is no preferred length scale for solute Rayleigh number $\lvert Ra_s\rvert\sim 10^3$ with the help of the vertical background density flux, defined in our case ($\partial_z T_0=0$) as [10,19] $F_z\equiv\rho_0[-\alpha(w_0T_0-\kappa_t\partial_z T_0)+\beta(w_0S_0-\kappa_s\partial_z S_0)]=\rho_0[-\alpha w_0T_0+\beta(w_0S_0-\kappa_s\partial_z S_0)]$. This flux can be written in the nondimensionalized form

$$F_z(\chi)=-w_0T_0+\frac{\mathrm{Gr}_s}{\mathrm{Gr}}\,w_0S_0+\frac{1}{H}\,\frac{16}{\mathrm{Ra}}\,\frac{\mathrm{Gr}_s}{\mathrm{Gr}}. \qquad (4.1)$$

This density flux [Eq. (4.1)] is a combination of convective fluxes (the first two terms on the right-hand side) and a diffusive flux (the last term, which is a constant since $\partial_z S_0$ is fixed in our analysis); the flux is upward if positive and downward if negative. Figure 7(a) shows the vertical density flux as a function of x for solute Rayleigh numbers $\lvert Ra_s\rvert>10^3$ for salty water ($H=10^2$ and $Pr=7$). Figure 7(b) is for solute Rayleigh number $\lvert Ra_s\rvert<10^3$. In Fig. 7(a), the flux for solute Rayleigh number $\lvert Ra_s\rvert>10^5$ is almost zero and the

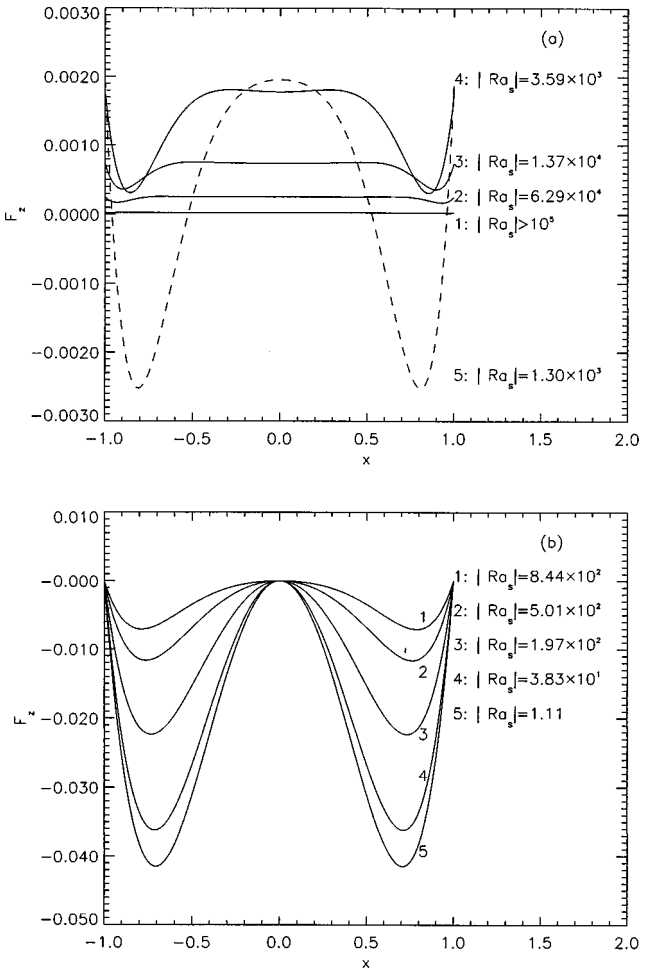

FIG. 7. Vertical background density flux for salty water ($H=10^2$, Pr=7) as a function of the solute Rayleigh number. The density flux is evaluated at the critical points. Panel (a) $F_z(x)$ [Eq. (4.1)] for solute Rayleigh numbers $|\mathrm{Ra}_s|>10^3$. Panel (b) $F_z(x)$ for solute Rayleigh numbers $|\mathrm{Ra}_s|<10^3$. For solute Rayleigh number $|\mathrm{Ra}_s|=1.3\times10^3$ (dashed line), we see that the denser fluid is transported upwards near the center and downwards near the wall. The restoring force from the lateral solute gradient plays a similar role here as the surface tension does in Rayleigh-Taylor instability. This provides another way of understanding the nonuniqueness of the critical wave number for $|\mathrm{Ra}_s|=1.3\times10^3$ in our doubly diffusive case.

instability is mainly due to dissipation and diffusion. In the double-diffusively-driven regime, as $|\mathrm{Ra}_s|$ decreases from 10^5 to 10^4, the background flow begins to grow in the interior of the channel and thus the critical wave numbers deviate significantly from those obtained within the asymptotic approximations. The critical length scale increases as $|\mathrm{Ra}_s|$ decreases because dissipation due to diffusion takes place over a larger length scale as a result of background shear flow throughout the slot. In Fig. 7(b) the density flux is negative and approaches the vertical slot convection limit as the solute Rayleigh number decreases below 10, confirming that in this regime the instability is shear induced. For $|\mathrm{Ra}_s|=1.3\times10^3$ in Fig. 7(a), the vertical density flux is positive at the center, transporting mass upwards. Near the boundary, the flux is negative, transporting mass downwards along the walls. Thus an overturning density flux is developed, moving

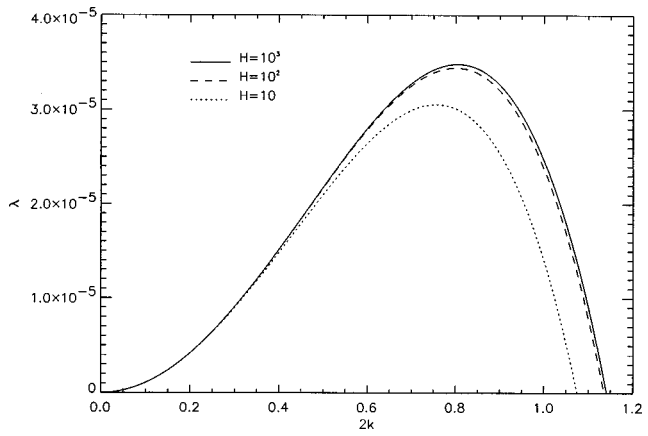

FIG. 8. The dependence of the growth rate (λ) of a disturbance on the wave number ($2k$) and on the solute diffusivity H at supercritical thermal Rayleigh number Ra=3.1 for $H=10$, Ra=0.31 for $H=10^2$ and Ra=0.031 for $H=10^3$ for a given solute Rayleigh number $|\mathrm{Ra}_s|=1.3\times10^3$. λ is measured in units of the circulation time (defined in Sec. II) and lengths are scaled by $d/2$. 33 modes are used in the calculations.

upwards near the center and spreading out downwards along the boundaries, with a restoring force due to the horizontal solute gradient playing the role of surface tension. Hence one would expect the instability for solute Rayleigh number $|\mathrm{Ra}_s|\sim10^3$ to be similar to Rayleigh-Taylor instability with surface tension, where the system can be unstable before too much energy is dissipated by diffusion or viscosity, and is unstable for disturbances over a range of wave numbers [11]. (In our case the system is unstable to perturbations of a finite range of wave numbers for any thermal Rayleigh number above the critical value Ra_c at $|\mathrm{Ra}_s|\sim1.3\times10^3$.) In Figure 8 we plot the growth rate (λ) as a function of wave number ($2k$) for $|\mathrm{Ra}_s|=1.3\times10^3$ at a supercritical thermal Rayleigh number Ra=3.1 for $H=10$, Ra=0.31 for $H=10^2$, and Ra=0.031 for $H=10^3$. (The critical thermal Rayleigh number $\mathrm{Ra}_c=2.91$ for $H=10$, $\mathrm{Ra}_c=0.291$ for $H=10^2$, and $\mathrm{Ra}_c=0.0291$ for $H=10^3$ for solute Rayleigh number $|\mathrm{Ra}_s|=1.3\times10^3$.) We remark that in vertical slot convection, the shear flow transports the fluid, and therefore the sign of the density flux is only indicative of the direction of transport of fluid, and does not imply that the fluid is top-heavy if the flux is negative or vice versa.

We now focus on the comparison between laterally driven double diffusive convection and thermohaline convection in a horizontal layer of fluid heated from below (henceforth, the ''thermohaline Rayleigh-Bénard convection'' case). With no solute, the critical states are stationary and supercritical in both cases. When adding a less diffusive, stably stratified solute into the system, different diffusivities provide channels of dissipation of energy on different time scales and thus oscillatory instability may set in before the stationary instability. In the thermohaline Rayleigh-Bénard case, the instability becomes oscillatory and subcritical with solute added [10,13]. In laterally driven diffusive convection, the instability remains stationary and supercritical for solute Rayleigh numbers smaller than the threshold values defined above, and as the solute Rayleigh number increases above the threshold value, the critical states become stationary and subcritical. As the solute Rayleigh number increases above 10^2

(still below 10^3), the background shear flow decreases significantly in amplitude [Fig. 7(b)]. The instability becomes oscillatory [dashed lines in Figs. 4(b), 5(a), and 5(b)]; the balance between the shear flow and the diffusion in this regime can be envisioned as follows. Imagine that a cell of fluid near the hot wall rises vertically from the bottom of the slot. Since heat diffuses much more efficiently than solute, we assume that this cell is in local thermal equilibrium with the background temperature field at all times. This cell will move horizontally to the cold wall due to the horizontal solute gradient, and it will sink downwards as it crosses the midplane to the other half of the tube. Because the shear flow is weak, the cell can move significantly towards the hot wall as soon as this cell is lighter than the ambient fluid at the same horizontal level. As it moves near the hot wall, it will rise again because now it is heated near the hot wall; thus oscillatory motion is established, and instability sets in as this oscillation is amplified. We further remark that for $|\mathrm{Ra}_s|$ smaller than 10^2 the shear flow is too strong for the oscillatory mode to set in before the stationary mode. For $|\mathrm{Ra}_s|$ greater than 10^4, the shear flow is too weak, and the instability sets in as a result of different diffusivities. The larger the solute diffusivity, the more stable the system is and thus the higher the critical Rayleigh number, as shown in Fig. 2. No Hopf bifurcations are found for the secondary instability listed in Table I. A reasonable flow chart can be constructed for each combination of states for the fixed points in the table as in [18], and we refer readers to [18] for more details.

V. CONCLUSION

We have formulated the laterally driven double diffusive convection problem without resorting to asymptotic approximations, and have solved it in both linear and weakly nonlinear regimes. The effect of different solute diffusivities in both the shear-induced regime and the double-diffusively-driven regime is investigated by exploring a wide range of parameters in our analyses. In the shear-induced regime [$\beta\Delta S/\alpha\Delta T \ll O(1)$], results show that different solute diffusivities change the characteristics of instability even though the stabilizing force is small compared to the background shear flow (small solute Rayleigh number $|\mathrm{Ra}_s|<10$).

In the double-diffusively-driven regime [$\beta\Delta S/\alpha\Delta T \geqslant O(1)$], results from our linear analyses agree well with those from the asymptotic approximations for $|\mathrm{Ra}_s|>10^5$. We also propose an explanation for the discrepancies between results from our weakly nonlinear analyses and those in [5] for $H=10$ and $H=10^2$. We provide a deeper understanding of doubly diffusive convection by comparing our results for double-diffusive slot convection to those in the thermohaline Rayleigh-Bénard convection. We point out the possible errors made in the determination of critical thermal Rayleigh numbers for solute Rayleigh numbers $2<-R_s<5$ in [7]; and using the vertical background density flux, we explain why no preferred length scale is present when $|\mathrm{Ra}_s| \sim 10^3$ for all diffusivity ratios by resorting to an analogy with Rayleigh-Taylor overturning instability in the presence of surface tension, where the system is unstable for disturbances over a limited range of wave numbers.

ACKNOWLEDGMENTS

We would like to thank J. Biello, F. Cattaneo, C. F. Chen, O. Kerr, N. Lebovitz, and J. Werne for helpful conversations. This work was supported in part by NASA and DOE grants to the University of Chicago.

[1] S. A. Thorpe, P. K. Hutt, and R. Soulsby, J. Fluid Mech. **38**, 375 (1969).
[2] J. Mizushima and K. Gotoh, J. Phys. Soc. Jpn. **52**, 1206 (1983).
[3] J. E. Hart, J. Fluid Mech. **49**, 279 (1971).
[4] C. F. Chen, J. Fluid Mech. **63**, 563 (1974).
[5] J. E. Hart, J. Fluid Mech. **59**, 47 (1973).
[6] R. C. Paliwal and C. F. Chen, J. Fluid Mech. **98**, 769 (1980).
[7] S. Thangam, A. Zebib, and C. F. Chen, J. Fluid Mech. **112**, 151 (1981).
[8] Y. Young and R. Rosner, Phys. Rev. E **57**, 1183 (1997).
[9] A. H. McAllister, Ph.D. thesis, The University of Texas at Austin (1991).
[10] G. Veronis, J. Fluid Mech. **34**, 315 (1968).
[11] S. Chandrasekhar, *Hydrodynamic and Hydromagnetic Stability* (Dover Publication, New York, 1981).
[12] C. Canuto, M. Y. Hussaini, A. Quarteroni, and T. A. Zang, *Spectral Methods in Fluid Dynamics* (Springer-Verlag, New York, 1988).
[13] P. H. Coullet and E. A. Spiegel, SIAM J. Appl. Math. **43**, 776 (1983).
[14] F. Cattaneo, Ph.D. thesis, Cambridge University (1980).
[15] E. Knobloch, Phys. Rev. A **34**, 1538 (1986).
[16] M. R. E. Proctor and C. A. Jones, J. Fluid Mech. **188**, 301 (1988).
[17] E. Knobloch and M. R. E. Proctor, Proc. R. Soc. London, Ser. A **415**, 61 (1988).
[18] J. Guckenheimer and P. Holmes, *Nonlinear Oscillations, Dynamical Systems, and Bifurcations of Vector Fields* (Springer-Verlag, New York, 1983).
[19] J. S. Turner, *Buoyancy Effects in Fluids* (University Press, Cambridge, 1973).